 doi:10.20944/preprints202010.0359.v1

Comparison of the structural evolution of β polypropylene during the sequential and simultaneous biaxial stretching process

Daoxin Zhang[1], Lei Ding[1], Feng Yang*[1], Fang Lan[1], Ya Cao[1], Ming Xiang[1],
[1]State Key Laboratory of Polymer Materials Engineering, Polymer Research Institute of Sichuan University, Chengdu, China

Daoxin Zhang
Email: daoxinz@163.com

Lei Ding
Email: dinglei921022@163.com

Feng Yang*
Email: yangfengscu@126.com

Fang Lan
Email: lf5347@sina.com

Ya Cao
Email: caoya@scu.edu.cn

Ming Xiang
Email: teylor112@163.com

***To whom correspondence should be addressed:**
Feng Yang**
Phone: 86-28-85403118
Fax: 86-28-85402465
Email: yangfengscu@126.com

 doi:10.20944/preprints202010.0359.v1

Comparison of the structural evolution of β polypropylene during the sequential and simultaneous biaxial stretching process

Daoxin Zhang[1], Lei Ding[1], Feng Yang*[1], Fang Lan[1], Ya Cao[1], Ming Xiang[1],

[1]State Key Laboratory of Polymer Materials Engineering, Polymer Research Institute of Sichuan University, Chengdu, China

Abstract

In this paper, the lamellar structural evolution and microvoids variations of β-iPP during the processing of two different stretching methods, sequential biaxial stretching and simultaneous biaxial stretching, were investigated in detail. It was found that different stretching methods led to significantly different lamellae deformation modes, and the microporous membranes obtained from the simultaneous biaxial stretching exhibited better mechanical properties. For the sequential biaxial stretching, abundant coarse fibers originated from the tight accumulation of the lamellae parallel to the longitudinal stretching direction, whereas the lamellae perpendicular to the stretching direction were easily deformed and separated. Those coarse fibers were difficult to be separated to form micropores during the subsequent transverse stretching process, resulting in a poor micropores distribution. However, for the simultaneous biaxial stretching, the β crystal had the same deformation mode, that is, the lamellae distributed in different directions were all destroyed, forming abundant microvoids and little coarse fibers formation.

Keywords: β-iPP, simultaneous biaxial stretching, sequential biaxial stretching, structure evolution

Introduction

Polymeric porous membranes have been widely applied in a broad range of oil-water separation, air purification, seawater desalination, and energy storage [1-5]. Compared with other polymers used to manufacture membranes, polypropylene (PP)

 doi:10.20944/preprints202010.0359.v1

has a unique advantage in terms of solvent resistance property, mechanical and processability properties as well as price. Currently, the most commonly used manufacturing process for PP microporous membrane is the “dry process”, which mainly includes the uniaxial stretching method and sequential biaxial stretching method [6-13]. While the uniaxial stretching method is difficult to achieve continuous production due to the treatment of precursor film and the microporous membrane prepared by this process has very low lateral mechanical properties. The sequential biaxial stretching process can avoid the above problems, so it is an ideal technology for preparing microporous membranes [14, 15]. However, the uneven pore size distribution of the membrane made by this process limits its application.

Many studies have been put into improving the performance of microporous membranes [16-23]. It has been found that the performance of the membrane can be tuned by changing stretching parameters, such as annealing temperature and tensile temperature, and tensile ratio. For example, Grant et al. [24] found that the films annealed near the melting temperature of β crystal exhibited larger porosity, suggesting that annealing perfected the crystalline structure, thereby contributing to the formation of pores. In our previous work, we found that annealing could not only thicken the lamellar thickness but also narrow the lamellar thickness distribution, thus improving the performance of membranes [25]. Yang et al. [26] succeeded in improving the pore size distribution by optimizing stretching temperature and tensile ratio. Except for the process parameters, the crystalline structure of precursor films also influences the performance of the membrane. Yang et al. [27] investigated the pore formation process of four kinds of precursor films with different supermolecular structures and found that the sample with well-developed spherulite structure was more conducive to form uniform pores after stretching. Moreover, Ding et al. [28] prepared four samples with different distributions of β-lamellae and revealed that the sample with lamellae almost all perpendicular to the stretching direction had homogenous deformation. Zhu et al. [29] found that the crystalline morphology changed from spherulites into β-transcrystals by adding ultrafine full-vulcanized powder rubber (EA-UFPR), and its loosely-packed lamellae facilitated the formation of micropores. Based on the previous

Preprints (www.preprints.org) | NOT PEER-REVIEWED | Posted: 19 October 2020 doi:10.20944/preprints202010.0359.v1

literature, it is not difficult to find that most of the studies mainly focus on improving the pore size distribution by improving the distribution of β-lamellae or changing the crystalline morphology of β-crystals by adding different additives, however, little attention has been paid to changing the stretching process.

Currently, the preparation of β-iPP microporous membranes mainly adopts a sequential biaxial stretching process, namely, the sample is first stretched along the machine direction (MD) and then along the transverse direction (TD). During the stretching process in the MD direction, the lamellae with different orientations relative to the tensile direction will lead to different modes of deformation, which ultimately affects the performance of the prepared microporous membrane [30-34]. Therefore, we envisage whether a novel simultaneous biaxial stretching process can be used to make the polydisperse β crystals exhibit the same deformation pattern, that is, the defects induced more uniformly, thereby improving the performance of the microporous membrane. In this article, a comparative study of the structural evolution process of β-iPP during sequential and simultaneous biaxial stretching was carried out using two-dimensional wide and small-angle X-ray diffraction (2D-WAXD and SAXS) and scanning electron microscopy (SEM). According to the relationship between the formation of microvoids and structural evolution, the deformation mechanism of β-iPP for two stretching methods was proposed, hoping to provide new inspiration for the manufacture of microporous membranes.

2. Experimental

2.1.1. Material

Isotactic PP (T38F) with a melt flow rate (MFR) of 3g/10min (230 °C, 21.6 N) was obtained from Lanzhou Petrochemical Incorporation. The β-nucleating agent (β-NA) pimelic acid and calcium stearate (Pa-Ca) was obtained by neutralization of pimelic acid ($C_7H_{12}O_4$, chemical pure reagent) and calcium stearate (chemical pure reagent) [35].

Preprints (www.preprints.org) | NOT PEER-REVIEWED | Posted: 19 October 2020 doi:10.20944/preprints202010.0359.v1

2.1.2. Precursor films preparation

A masterbatch containing 5 wt% β-NA was prepared through melt blending, and then the masterbatch was melt blended with additional iPP to obtain a sample containing 0.3 wt% β-NA. The sample was used to produce pellets using a twin-screw extruder. After pelletizing, the β-iPP precursor films were prepared by a Haake single screw extruder at 230 °C and the surface temperature of the chill roll was maintained at 126 °C.

2.1.3. Microporous membrane preparation

The β-iPP membranes were prepared using a biaxial stretcher KARO IV (Brückner, Germany). The precursor films were cut into 90 mm (length) × 90 mm (width) × 0.9 mm (thickness) to facilitate stretching. For the sequential biaxial stretching process, the precursor films were firstly stretched to a draw ratio of 1×3 at 90 °C after being preheated for 2 min, and then the films were moved to a chamber of 125 °C to be stretched to the final ratio of 3×3. For the simultaneous biaxial stretching process, the films were firstly stretched to 1.5×1.5 at 90 °C, and then were moved to the second chamber for further stretching to 3×3 at 125 °C. For easier description, the naming of these specimens was simplified as the iPP-seq-draw ratio or iPP-sim-draw ratio. For instance, when the sample was simultaneously stretched to 3×3, it was named by iPP-sim-3×3.

2.2. Measurements

2.2.1. Differential scanning calorimetry (DSC)

The thermal analysis was tested on a machine of Mettler Toledo DSC1 (Switzerland). A sample of about 2-5 mg was heated from room temperature to 200 °C at 10 °C/min under a nitrogen atmosphere (50 ml/min). The crystallinity (X_{DSC}) was defined as follows:

Preprints (www.preprints.org) | NOT PEER-REVIEWED | Posted: 19 October 2020 doi:10.20944/preprints202010.0359.v1

$$X_{DSC} = \frac{\Delta H_{sam}}{\Delta H_{id}} \times 100\ \% \quad (1)$$

where ΔH_{sam} was the heat of fusion of samples, and ΔH_{id} was the fusion enthalpy of 100 % crystalline sample. The value of ΔH_{id} was 177.0 J/g for α crystals and 168.5 J/g for β crystals [36]. The relative fraction of β crystal ($K_{\beta, DSC}$) could be obtained by the Eq. (2):

$$K_{\beta,DSC} = \frac{X_{c\beta}(\%)}{X_{c\alpha}(\%)+X_{c\beta}(\%)} \times 100\ \% \quad (2)$$

in which $X_{c\alpha}(\%)$ and $X_{c\beta}(\%)$ were the degrees of crystallinity for α crystals and β crystals, respectively.

2.2.2. SEM tests

Surface morphology and supermolecular structure were characterized by using an FEI Inspect F SEM with an accelerating voltage of 10 kV. To observe the supermolecular structure, the samples were etched for 8 hours at 0 °C using a mixed acid solution containing H_3PO_4-H_2SO_4-$KMnO_4$ for observing the morphology of crystal regions [37].

2.2.3. 2D-SAXS measurement

SAXS tests were performed on a Xeuss system of Xenocs France and the distance between sample and detector was 2500 mm. The parameters of the scattering geometry were calibrated with silver behenate as the standard. The SAXS images were recorded by the Pilatus 300 K detector of Dectris, Switzerland. The long period (L_p) was estimated using the Bragg equation[38]:

$$L_P = \frac{2\pi}{q_{peak}} \quad (3)$$

where q_{peak} corresponded to the maximum value of the 1D integration curves (Iq^2 = f(q)). The crystalline thickness (L_c) and amorphous layer thickness (L_a) was derived from the following formula:

Preprints (www.preprints.org) | NOT PEER-REVIEWED | Posted: 19 October 2020 doi:10.20944/preprints202010.0359.v1

$$L_c = L_p \frac{\rho}{\rho_c} X_c \quad (4)$$

$$\frac{1}{\rho} = \frac{x_c}{\rho_c} + \frac{1-x_c}{\rho_a} \quad (5)$$

where ρ_c (0.95 g/cm^3) was the crystalline density and ρ_a (0.865 g/cm^3) was amorphous density.

2.2.4. 2D-WAXD measurement

The 2D-WAXD measurements were performed on a Japan Rigaku HomeLab diffractometer with a CuKα radiation (wavelength λ=0.154nm). An image plate (IP) detector (pixel size 100 μm) was used to record 2D-WAXD patterns. 1D-WAXD curves were obtained from 2D-WAXD patterns by circular integration. The relative percentage of β crystal ($K_{\beta\text{-}WAXD}$) was calculated by the equation [39]:

$$K_{\beta-WAXD} = \frac{A_{\beta(300)}}{A_{\alpha(110)}+A_{\alpha(040)}+A_{\alpha(130)}+A_{\beta(300)}} \times 100\ \% \quad (6)$$

where $A_{\beta(300)}$ was the area of the β(300) diffraction peak; $A_{\alpha(110)}$, $A_{\alpha(040)}$, and $A_{\alpha(130)}$ were the areas of diffraction peaks belonging to the α-crystal plane. The crystallinity ($X_{c\text{-}WAXD}$) and were evaluated as follows:

$$X_{XRD} = \frac{\sum A_{cry}}{\sum A_{cry}+\sum A_{amo}} \times 100\ \% \quad (7)$$

where A_{cry} and A_{amo} were the areas of the crystalline and amorphous phase in the WAXD pattern, respectively. Besides, the 1D-WAXD intensity profiles of α(040) and β(300) were obtained from the integration along the azimuthal angle. The orientation parameter of crystalline ($f_{\alpha(040)}$) was estimated by Herman orientation function [40]:

$$f_{\alpha(040)} = \frac{3<cos\varphi^2>-1}{2} \quad (8)$$

where φ was the angle between the tensile direction (MD) and the normal direction of the (040) crystal plane. $f_{\alpha(040)}$ = 1 meant that all lamellae were perpendicular to the tensile direction, while $f_{\alpha(040)}$ = 0 represented a random orientation situation.

Preprints (www.preprints.org) | NOT PEER-REVIEWED | Posted: 19 October 2020 doi:10.20944/preprints202010.0359.v1

2.2.5. Mechanical tests

The mechanical analysis of the membranes was carried out on an MTS universal tensile testing machine. The procedure used referred to the GB/T1040.3–2006 standard.

2.2.6. Porosity determination

The porosity was calculated by measuring the weight of the sample before and after soaking in butanol for 6 hours from the following equation [41]:

$$\Phi_i = \frac{(W_0 - W)\rho_0}{\rho_0 W_0 - (\rho - \rho_0)W} \times 100\% \quad (9)$$

where W and W_0 were the sample weight before and after immersion in butanol. ρ (0.8 g cm^{-3}) and ρ_0 (0.91 g cm^{-3}) were the density of butanol and PP, respectively.

3. Results and discussion

3.1. Crystal structure characterization of cast film

The 2D-WAXD and 2D-SAXS patterns of cast film were shown in Fig. 1a and b. From the 2D-WAXD pattern, two randomly oriented diffraction rings correspond to β(300) and β(301) (from inner to outer) were observed. Two predominant diffraction peaks at 2θ=16.1° and 2θ=21.1° originating from β(300), β(301) were observed in the 1D-WAXD intensity curve. The characteristic diffraction peaks of α crystal were almost undetectable, revealing that the cast film was almost entirely composed of β crystal. Moreover, the relative fraction of β crystal was about 99.3 % and the total crystallinity was estimated as 56.5 %. For the 2D-SAXS pattern, the isotropic scattering ring also proved randomly oriented lamellae stacks of cast film. Based on the corresponding 1D-SAXS intensity profile, the long spacing (L_p), the thickness of crystalline (L_c), and the amorphous layer (L_a) were shown in Table 1.

Fig. 1c showed the melting behavior of the cast film. Two basic melting peaks were observed in the DSC curve. The stronger peak at about 149 °C was attributed to

Preprints (www.preprints.org) | NOT PEER-REVIEWED | Posted: 19 October 2020 doi:10.20944/preprints202010.0359.v1

the melting of β crystal, while the weaker peak at about 167.5 °C was due to the melting of α crystal. For comparison, $X_{c\text{-}DSC}$ and $K_{\beta\text{-}DSC}$ calculated from DSC data was also provided in Table 1, which was slightly lower than the one calculated from 1D-WAXD due to the recrystallization process during heating.

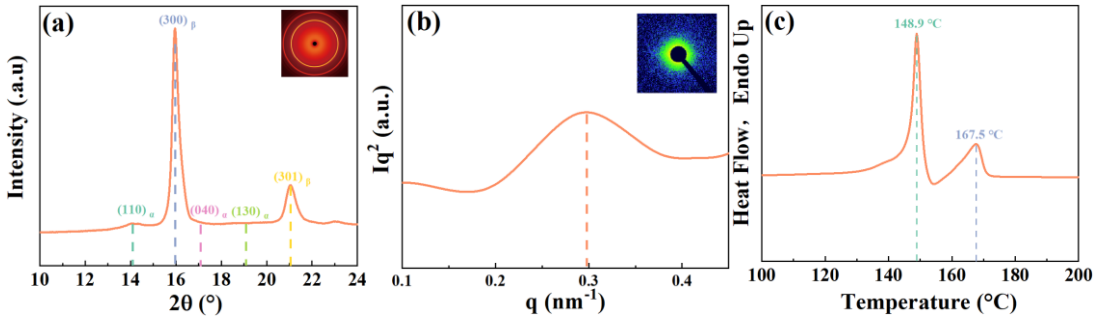

Fig. 1. (a) 1D-WAXD curve of β-iPP precursor film with the 2D-WAXD pattern. (b) Lorentz corrected 1D- SAXS intensity profile with 2D-SAXS patterns. (c) Heat flow curve of β-iPP.

Table 1 Microstructural parameters of β-iPP.

Sample	L_p (nm)	L_c (nm)	L_a (nm)	$X_{c\text{-}WAXD}$ (%)	$K_{\beta\text{-}WAXD}$ (%)	$X_{c\text{-}DSC}$ (%)	$K_{\beta\text{-}DSC}$ (%)
β-iPP	21.1	11.4	9.7	56.5	99.3	45.8	84.3

Fig. 2 showed the surface and cross-sectional crystal morphology of the cast film. The morphology of the center region (region A) of the β crystals reflected its nucleation mode, that was, the lamellar bundle was the initial growth mode of β crystals, namely the edge-on lamellae (red region). With the lamellar growth, branching and proliferation of lamellae took place, producing the flat-on lamellae (blue region).

Preprints (www.preprints.org) | NOT PEER-REVIEWED | Posted: 19 October 2020 doi:10.20944/preprints202010.0359.v1

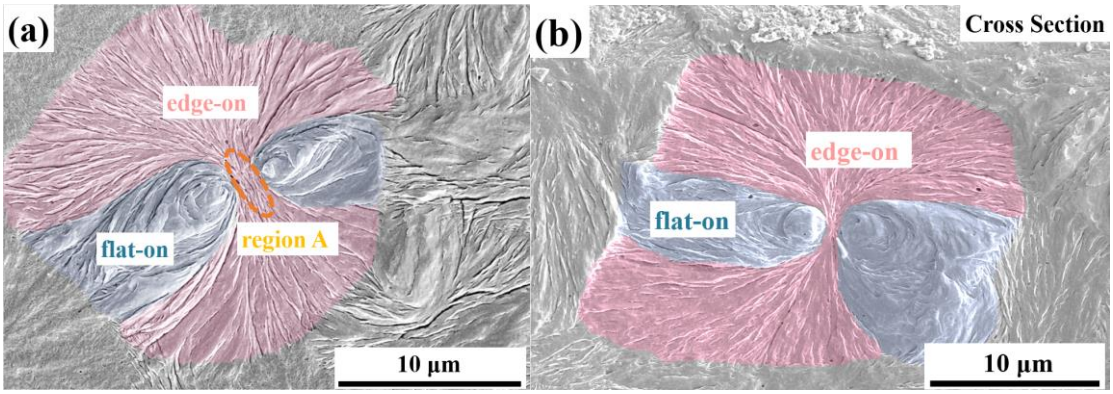

Fig. 2. SEM images of β-iPP: (a) surface section; (b) cross-section.

3.2. The stress-strain curves of β-iPP during the biaxial stretching process

Fig. 3 showed the stress-draw ratio behavior of β-iPP during the simultaneous biaxial stretching process at 90 °C. The yield stress of β-iPP along MD and TD was about 3.3 MPa. The stress-draw ratio curves could be divided into three regions, which were elastic deformation and yielding region to the draw ratio (DR) about 1.5 (region I), a plateau region from 1.5 to about 2.2 (region II), and a strain-hardening region up to 3 (region III). Hence, the selected tensile ratios for simultaneous biaxial stretching were set at 1.2×1.2, 1.5×1.5, 2.2×2.2, 2.5×2.5, and 3×3.

To verify whether the simultaneous biaxial stretching could directly obtain the microporous membrane, Fig. 3a showed the surface morphology of the cast film stretched to 3×3. It could be seen that there were abundant dense regions (region A in Fig. 3b), and a small number of micropores were formed (region B in Fig. 3b). Hence, it was not feasible to prepare a microporous membrane by a one-step biaxial stretching method. Some authors also believed that the formation of micropores includes two stages, that is, the pore creation at low temperature and then pores growth at high temperature [42]. Hence, the simultaneous biaxial stretching process also used two temperatures for stretching.

Preprints (www.preprints.org) | NOT PEER-REVIEWED | Posted: 19 October 2020 doi:10.20944/preprints202010.0359.v1

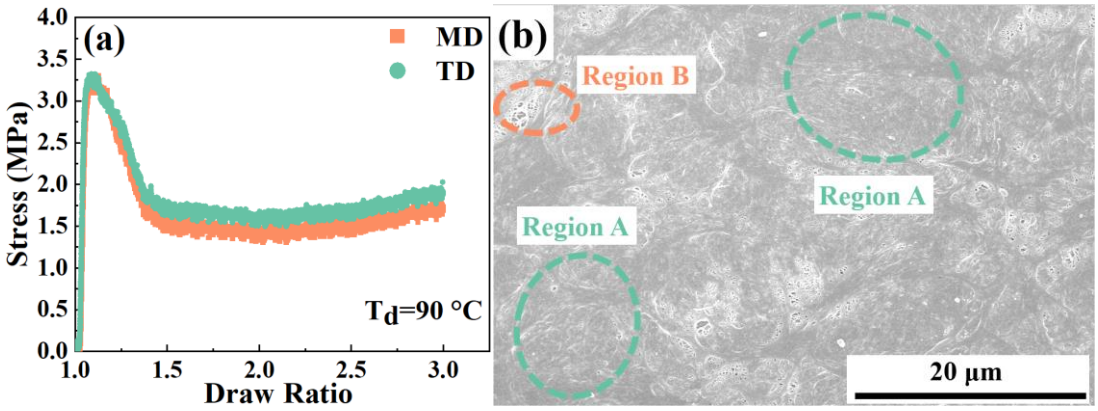

Fig. 3. (a) stress-draw ratio curves of β-iPP during simultaneous biaxial stretching. (b) SEM image of the prepared membrane.

Fig. 4 showed the stress-strain curves of the sequential and simultaneous biaxial stretching process. In the first step of sequential biaxial stretching (longitudinal stretching to 3×1 at 90 °C), the MD curve showed a faint stress drop and a rather steady yield peak. This was related to the uniform plastic deformation on the macroscopic scale, which was observed from the uniform decrease of the specimen width with an increase of draw ratio. Strain hardening appeared at a high draw ratio for the MD curve, which meant that some fibrillar structure developed during the first stretching [36]. In the second step of the sequential biaxial stretching (transverse stretching to 3×3 at 125 °C), the TD curve showed low yielding stress and extremely weak yield peak. Because the fiber structure formed after stretching along MD had numerous defects distributed among it, making it easier to separate and deformation during the transverse stretching (shown in Fig. 9d). For the simultaneous biaxial stretching process, the balanced stress-strain curves in each direction indicated the uniform deformation of the sample during stretching. Besides, both MD and TD curves showed typical yielding and strain-hardening behavior, which meant that the original structures were destroyed and then the newly formed structure oriented in MD and TD plane direction [33].

Preprints (www.preprints.org) | NOT PEER-REVIEWED | Posted: 19 October 2020 doi:10.20944/preprints202010.0359.v1

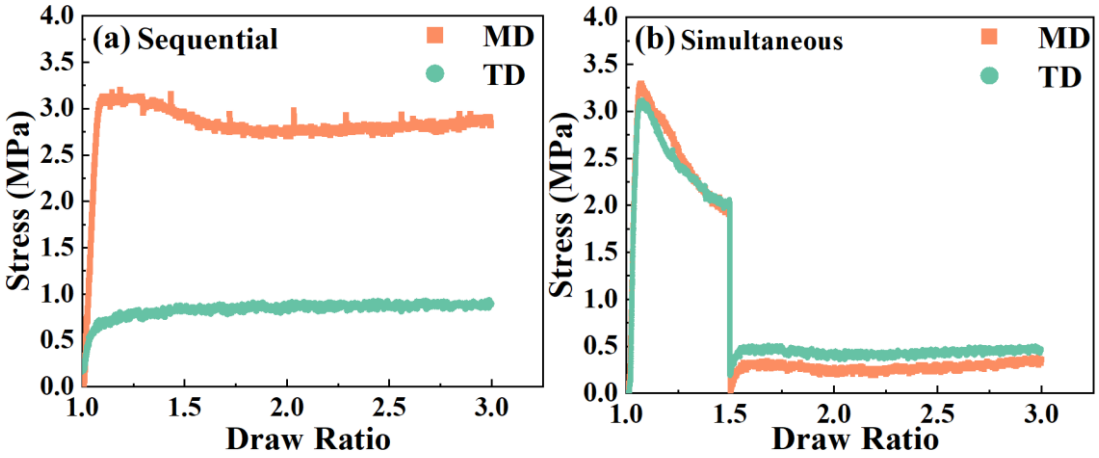

Fig. 4. Stress-strain curves of β-iPP: (a) sequential biaxial stretching; (b) simultaneous biaxial stretching.

3.3. 2D-SAXS and 2D-WAXD analysis results during stretching

To investigate the pore formation and structure evolution during stretching, Fig. 5 showed the selective 2D-SAXS patterns. For the sequential biaxial stretching, the stretched sample showed significant cavities signal in the meridian direction at the beginning of stretching. The scattering streak was along the stretching direction, indicating the orientation of initial cavities were along the stretching direction. With further deformation, the direction of the streak was perpendicular to the stretching direction, which implied the reorientation of cavities. For simultaneous biaxial stretching, the scattering signal of cavities was initially subcircular. Moreover, the shape of the cavities signal did not change during further stretching, which indicated that the cavities were randomly oriented.

Preprints (www.preprints.org) | NOT PEER-REVIEWED | Posted: 19 October 2020 doi:10.20944/preprints202010.0359.v1

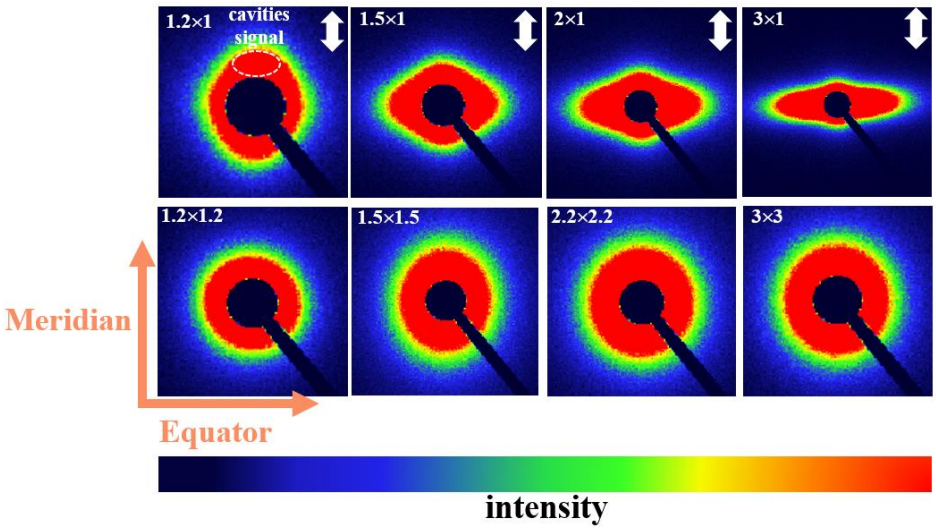

Fig. 5. Selective 2D-SAXS patterns of β-iPP during sequential and simultaneous biaxial stretching.

To better study the variation of cavities during two stretching methods, the 1D-SAXS profiles along meridional and equatorial were shown in Fig. 6. For the sequential biaxial stretching, the cavities intensity on the meridian increased and reached its maximum at DR=2×1, and it gradually decreased in further deformation. However, the intensity on the equator kept increasing and its intensity was higher than in the meridian under the low draw ratio (DR<1.5×1). This indicated that normal initial cavities were parallel to the stretching direction, and then microvoids expanded and gradually oriented along the stretching direction.

For simultaneous biaxial stretching, the cavities intensity on the meridian and equator were not much diverse at the beginning of stretching. With further stretching, the intensity of cavities increased and there was little difference for the meridian and equator. This indicated that the cavities were randomly oriented during the stretching. These data demonstrated that different stretching methods would cause different pore formation and growth processes.

Preprints (www.preprints.org) | NOT PEER-REVIEWED | Posted: 19 October 2020 doi:10.20944/preprints202010.0359.v1

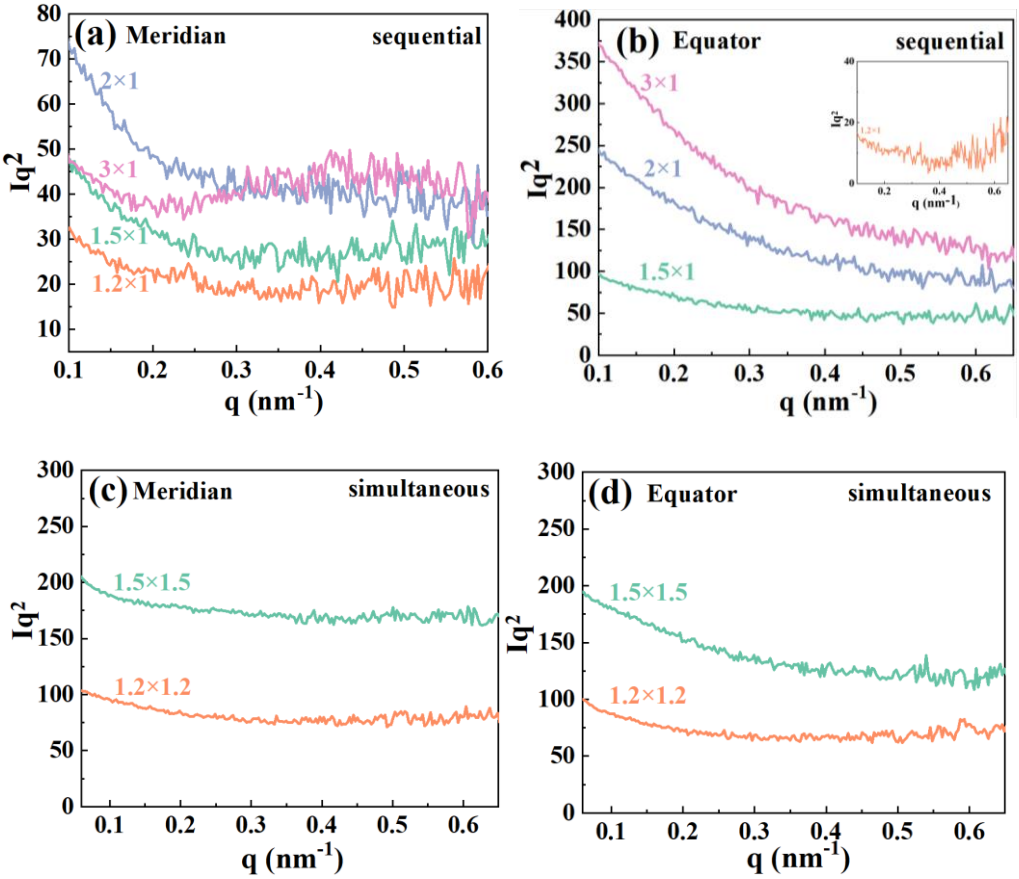

Fig. 6. Lorentz corrected 1D SAXS profiles of deformed β-iPP along the meridian and equator: (a) and (b) iPP-seq; (c) and (d) iPP-sim.

Fig. 7 showed the selective 2D-WAXD patterns during the sequential and simultaneous biaxial process. The two brightest diffraction rings corresponded to β(300) and β(301) (from inner to outer). For the two stretching methods, the variation of 2D-WAXD patterns was distinctly different. For the sequential biaxial stretching process, the scattering signal from β(300) on the equator weakened firstly and the scattering signal of α crystal planes appeared on the equator. Besides, it was noteworthy that the diffraction intensity of β(300) on the meridian was only slightly reduced at the same draw ratio, indicating that β crystal perpendicular to the stretching direction was more easily converted into the α crystal. With further stretching, the diffraction signal of β crystal vanished and the diffraction signal of α crystal tended to focus their intensity on the equator. It demonstrated that the newly formed α-crystal perpendicular to the stretching direction. However, for the simultaneous biaxial stretching process, the

Preprints (www.preprints.org) | NOT PEER-REVIEWED | Posted: 19 October 2020 doi:10.20944/preprints202010.0359.v1

scattering signal of β(300) was uniformed weakened, and the newly emerging scattering signal of α crystal planes was homogeneously distributed. This indicated that the β lamellae at different angles were deformed.

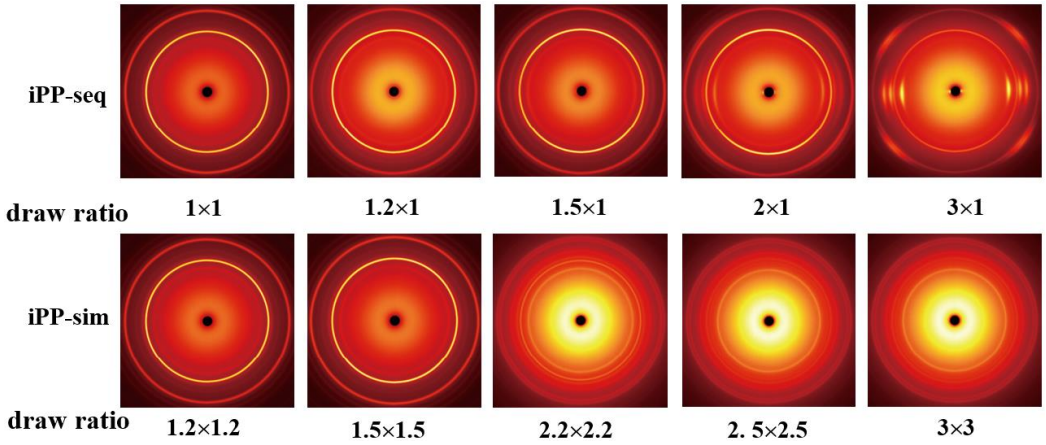

Fig. 7. Selected 2D-WAXS patterns of iPP during the sequential and simultaneous biaxial process. The stretching direction is vertical.

Fig. 8 showed the 1D-WAXD intensity profiles along the azimuthal angle of β(300) and α(040) crystal plane. The azimuthal angle of 0 ° or 180 ° was along the equator ($\beta_{\perp}$) and 90 ° or 270 ° was along the meridian ($\beta_{//}$). For the sequential biaxial stretching process, the intensity of the β lamellae perpendicular to the MD firstly weakened, while the intensity of the β lamellae parallel to the MD only slightly weakened. The 040 plane was along the b-axis of unit crystal cells and the corresponding 1D-WAXD curves showed increasingly pronounced peaks with stretching at 180 ° (as shown in Fig. 8c), which indicated an increase in orientation degree (the data shown in Fig. 8e).

However, for the simultaneous biaxial process, the azimuthal curves of β(300) iPP-sim always remained flat during stretching, which indicated that the lamellae in different directions deformed simultaneously. And the azimuthal curves of α(040) showed no obvious peaks, which indicated almost no orientation (the data shown in Fig. 8f).

Preprints (www.preprints.org) | NOT PEER-REVIEWED | Posted: 19 October 2020 doi:10.20944/preprints202010.0359.v1

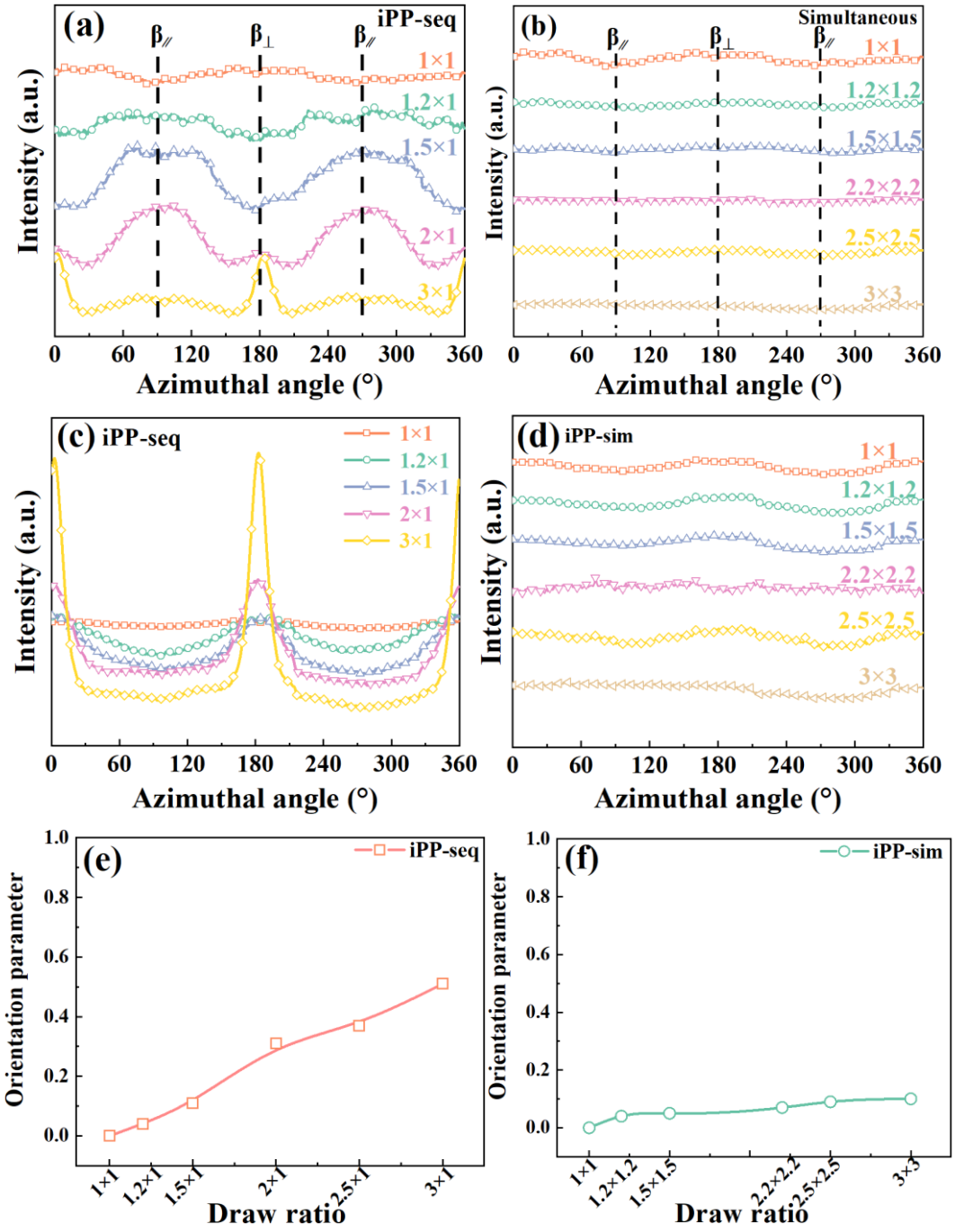

Fig. 8. 1D-WAXD intensity profiles of samples obtained from β (300) integration along azimuthal angle: (a) iPP-seq and (b) iPP-sim; 1D-WAXD intensity profiles of samples obtained from α (040) integration: (c) iPP-seq and (d) iPP-sim; (f) Herman orientation parameter: (e) iPP-seq and (f) iPP-sim.

3.4. Inspection of pore variation by SEM during the first stretching stage

To observe the pore initiation and the evolution of the internal structure intuitively,

Preprints (www.preprints.org) | NOT PEER-REVIEWED | Posted: 19 October 2020 doi:10.20944/preprints202010.0359.v1

Fig. 9 showed the surface and cross-sectional morphology of iPP-seq samples stretched to different draw ratios by using SEM. Interestingly, two completely different deformation modes were induced during stretching along MD due to the polydispersity of β lamellae. The bundle-like lamellae parallel to the stretching direction: some horizontal crazes (region A in Fig. 9a_1) mainly appeared between the deflected lamellae which were perpendicular to the stretching direction. However, no defects were observed in the lamellae parallel to the stretching direction (region B in Fig. 9a_1). And the flat-on lamellae were too rigid to be destroyed at a small draw ratio. With the draw ratio increased (DR=1×1.5), the flat-on lamellae were destroyed, forming abundant crazes (region B in Fig. 9a_2). Then those crazes were enlarged with further deformation and the orientation of those crazes were deflected in the MD, which corresponded to the SAXS results (as shown in Fig. 5). Moreover, some adjacent crazes joined together to form a bigger defect. Interestingly, the center lamellae of the crystal (region B in Fig. 9a_3) remained intact regardless of the stretching ratio. This was because the lamellae could not move until the neighboring lamellar movement, therefore, they would pack more densely, and the phase transformation occurred, forming coarse fibrils (region B in Fig. 9c).

The bundle-like lamellae perpendicular to the stretching direction: the lamellae at the center of the crystal were separated violently, forming slender crazes (region C in Fig. 9b_1). As the draw ratio increased (DR=1×1.5), more slender crazes appeared in the center of the spherulites (region C in Fig. 9b_2). Then a larger deformation band formed throughout the whole spherulite (region C in Fig. 9b_3), and the orientation of this preferred to the MD direction. Finally, this structure would not form the coarse fibers (region B in Fig. 8d). Moreover, the cross-sectional SEM images (Fig. 9d and e) also demonstrated that β-crystal with different orientations relative to the stretching direction would exhibit different deformation modes and form different structures during uniaxial stretching.

Preprints (www.preprints.org) | NOT PEER-REVIEWED | Posted: 19 October 2020 doi:10.20944/preprints202010.0359.v1

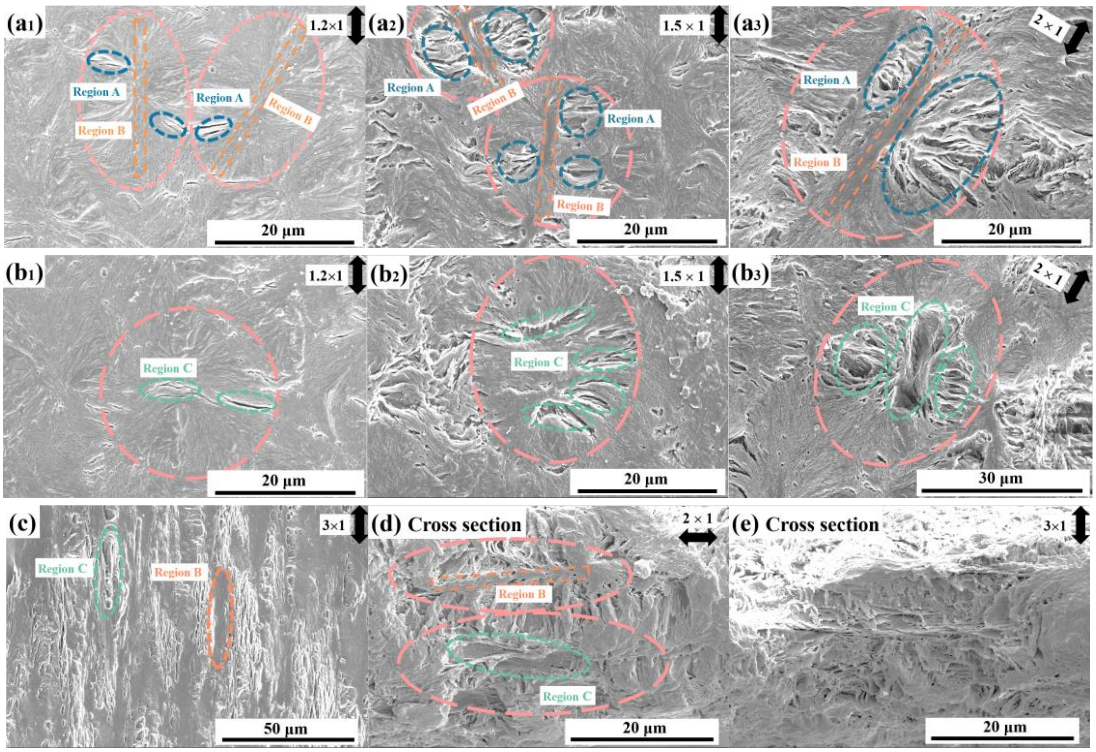

Fig. 9. SEM images of stretched iPP-seq: (a), (b) and (c) surface morphology of specific draw ratio; (d) and (e) cross-sectional morphology of stretched samples. The arrow indicated the loading direction.

Fig. 10 showed the evolution of the surface and cross-section morphology of the iPP-sim samples during the first stretching stage. Interestingly, despite the polydisperse nature of β-lamellae, the β crystals of iPP-sim showed the same deformation modes. Firstly, abundant crazes were predominately observed in the center region of the spherulites. Compared with the edge-on lamellae, the flat-on lamellae were too rigid to be deformed at first. Hence, substantial β-lamellae in region A were violently destroyed, leaving plenty of deformation bands. With further deformation (DR=1.5×1.5), the lamellae in the central region were further destroyed under the biaxial stress, leaving fragment blocky crystal structure. Also, the evolution of the cross-section morphology proved this deformation mode, which was also validated with the results of 2D-SAXS and 2D-WAXD.

Preprints (www.preprints.org) | NOT PEER-REVIEWED | Posted: 19 October 2020 doi:10.20944/preprints202010.0359.v1

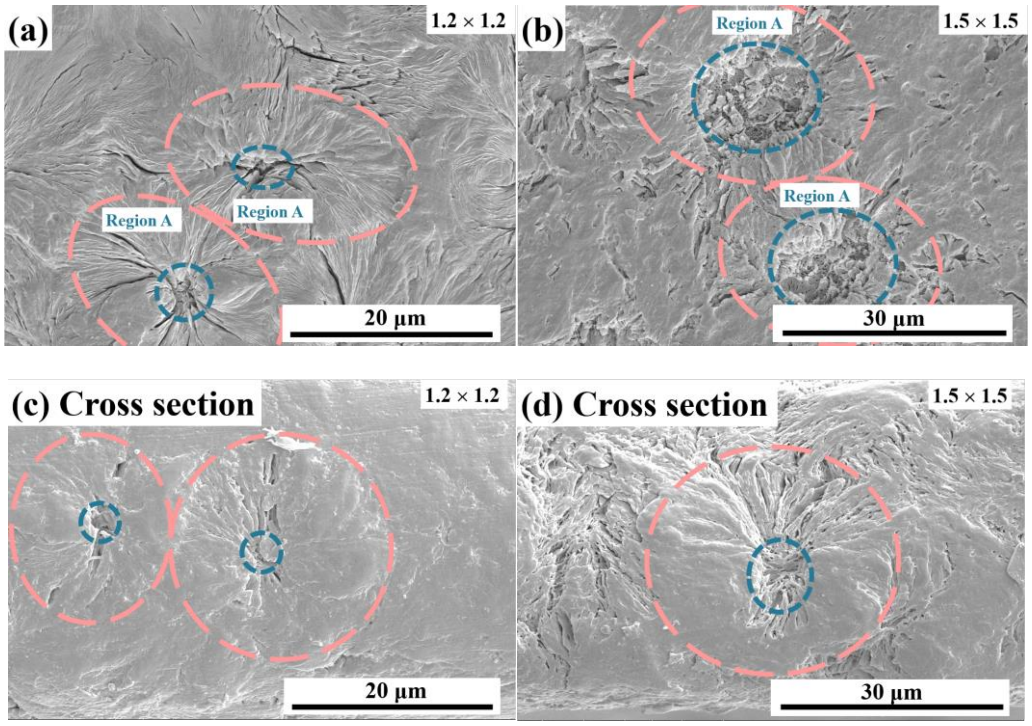

Fig. 10. SEM images of iPP-sim: (a) and (b) surface morphology; (c) and (d) cross-sectional morphology.

3.5. Analysis of pore growth during the second stretching stage

Fig. 11 showed the surface morphology of iPP-seq at different transverse draw ratio. The abundant microporous structure was formed by directly separating of the microfibrils. However, there were still large solid areas until the end of the transverse stretching, which was caused by the difficulty of separating the coarse fibers.

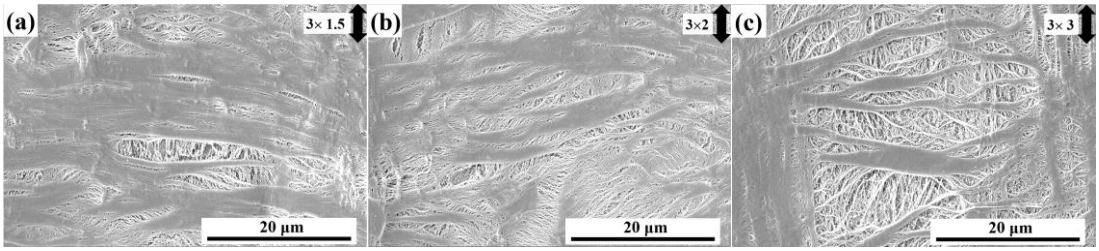

Fig. 11. SEM images of the iPP-seq after transverse stretching.

Fig. 12 showed the surface morphology of iPP-sim at different draw ratios. As the stretching process proceeded, the lamellar structure located at the region A was

Preprints (www.preprints.org) | NOT PEER-REVIEWED | Posted: 19 October 2020 doi:10.20944/preprints202010.0359.v1

continually subjected to the applied stress, resulting in the lamellar structure fragment and gradual evolution into a long-strip structure. Then, the long-strip structure converted into a randomly oriented microfibril structure and microvoids had formed between those fibrils by directly separating of the microfibrils. Finally, a microporous membrane was successfully prepared with almost no coarse fibers.

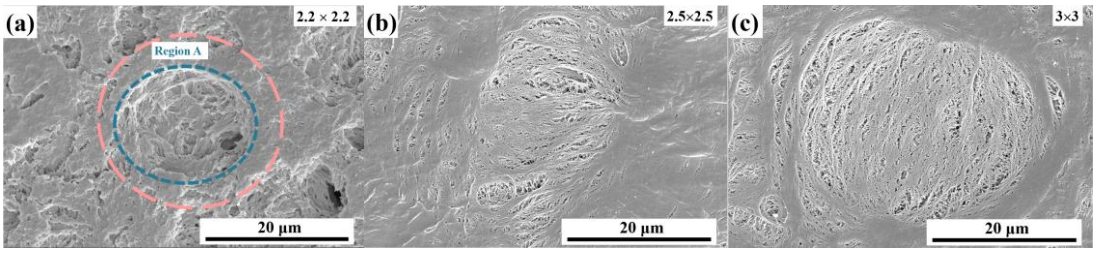

Fig. 12. SEM images of iPP-sim at different draw ratios.

To compare the mechanical properties of the two membranes, Fig. 13 showed the stress-strain curves. The stress-strain pattern was influenced by the biaxial stretching process. The simultaneous biaxial membrane had a balanced tensile property pattern and superior mechanical strength. Besides, the surface pore size distribution of the membranes was analyzed by the dedicated software (image J) [43]. For the membrane obtained by the simultaneous biaxial stretching process, the pore size distribution was narrower. The corresponding properties of the two membranes were shown in Table 2.

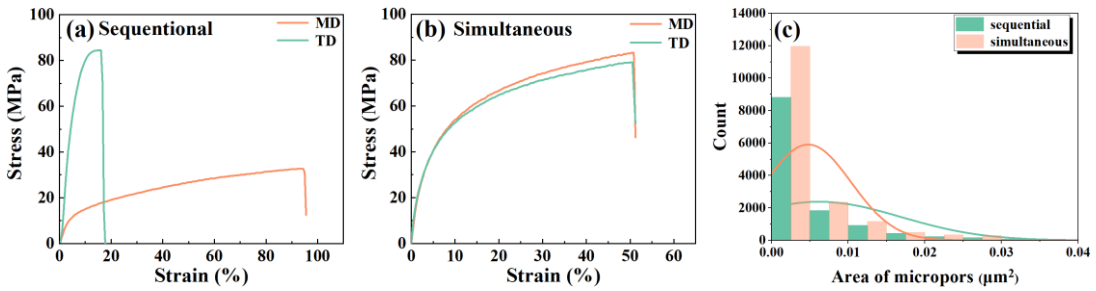

Fig. 13. Tensile properties of microporous membranes: (a) iPP-seq and (b) iPP-sim. (c) The pore size distribution of the two membranes.

Preprints (www.preprints.org) | NOT PEER-REVIEWED | Posted: 19 October 2020 doi:10.20944/preprints202010.0359.v1

Table 2 Physical properties of two microporous membranes.

Sample	iPP-seq	iPP-sim
Gurley (s/100ml)	440	380
Porosity (%)	42	48
Tensile strength (MD) (MPa)	85	80
Tensile strength (TD) (MPa)	30	75

3.6. The pore formation mechanism for two stretching methods.

Based on the above analysis, the mechanisms for two different stretching methods of pore formation and structural evolution were summarized in Fig. 14. For sequential biaxial stretching, the polydisperse β lamellae showed different deformation modes during MD stretching, the lamellae parallel to the MD packed more densely, forming coarse fibers, while the lamellae perpendicular to the MD were easily destroyed, leaving abundant defects between microfibers. Those coarse fibers hindered the micropores formation during TD stretching, causing inferior pore size distribution. However, for simultaneous biaxial stretching, the β lamellae were deformed in the same mode, forming abundant micropores with little coarse fibers.

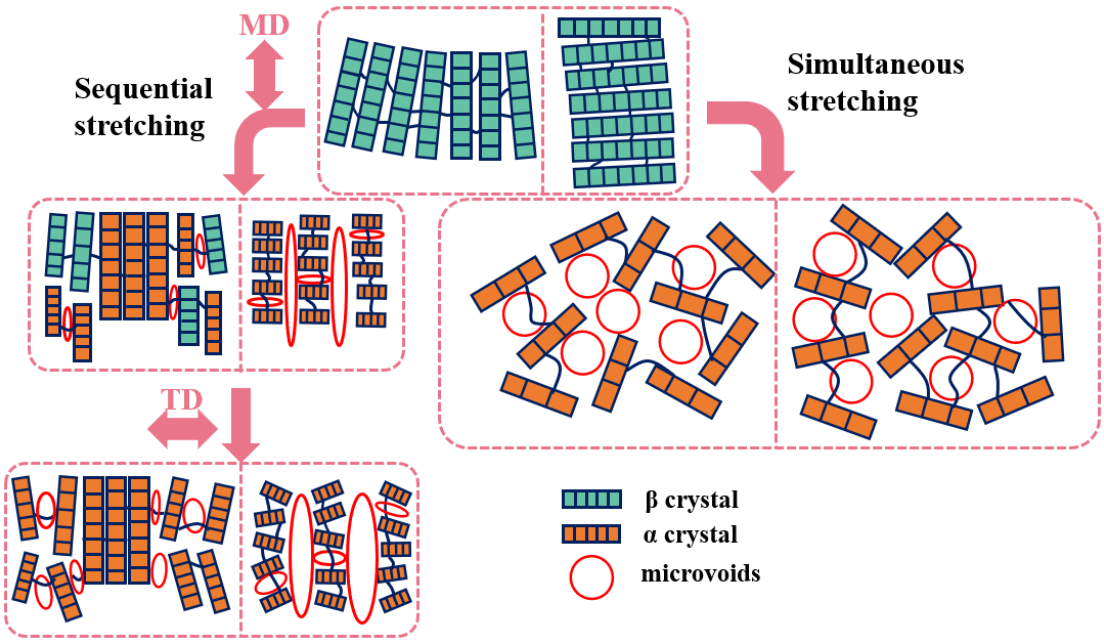

Fig. 14. Schematic model of structural evolution of β-iPP for two stretching methods.

 doi:10.20944/preprints202010.0359.v1

4. Conclusion

In this article, a comparative study of the structural and morphological evolution of β-iPP processed by two different stretching methods, including sequential biaxial stretching and simultaneous biaxial stretching, was carried out. The results of 2D-SAXS and 2D-WAXD during stretching showed that the samples had a significant difference in deformation modes for two stretching methods. For sequential biaxial stretching, the β lamellae at different angles relative to the stretching direction showed different ways of deformation, namely, the lamellae perpendicular to the stretching direction were easily deformed and separated, while the lamellae parallel to the stretching direction were packed densely and transformed into coarse fibers, which were difficult to be pulled apart during the second transverse stretching process, hindering the formation of micropores. However, for the simultaneous biaxial stretching, the polydisperse β lamellae had the same deformation mode, namely the center lamellae were firstly destroyed, and then the surrounding lamellae were destroyed, finally, abundant microvoids were formed, and nearly no coarse fiber was formed. The pore size distribution and mechanical test also proved that the microporous membrane obtained by the simultaneous biaxial stretching process had superior properties.

Acknowledgment

We would like to express our sincere thanks to the Natural Science Foundation of China for Financial Support (51721091).

Conflict of interest

The authors declare no potential conflict of interest.

References

1. Costa C. M.; Lee Y.-H.; Kim J.-H.; Lee S.-Y.; Lanceros-Méndez S. Recent

 doi:10.20944/preprints202010.0359.v1

advances on separator membranes for lithium-ion battery applications: From porous membranes to solid electrolytes. *Energy Storage Materials* **2019**, 22, 346-375.

2. Li Y.; Pan G.; Wang J.; Zhang Y.; Shi H.; Yu H.; Liu Y. Tailoring the Polyamide Active Layer of Thin-Film Composite Forward Osmosis Membranes with Combined Cosolvents during Interfacial Polymerization. *Industrial & Engineering Chemistry Research* **2020**, 59, 8230-8242.
3. Pan L.; Wang H.; Wu C.; Liao C.; Li L. Tannic-Acid-Coated Polypropylene Membrane as a Separator for Lithium-Ion Batteries. *ACS Appl Mater Interfaces* **2015**, 7, 16003-16010.
4. Park S.-H.; Kwon S. J.; Shin M. G.; Park M. S.; Lee J. S.; Park C. H.; Park H.; Lee J.-H. Polyethylene-supported high performance reverse osmosis membranes with enhanced mechanical and chemical durability. *Desalination* **2018**, 436, 28-38.
5. Zhu X.; Tang X.; Luo X.; Cheng X.; Xu D.; Gan Z.; Wang W.; Bai L.; Li G.; Liang H. Toward enhancing the separation and antifouling performance of thin-film composite nanofiltration membranes: A novel carbonate-based preoccupation strategy. *J. Colloid Interface Sci.* **2020**, 571, 155-165.
6. Lu W.; Yuan Z.; Zhao Y.; Zhang H.; Zhang H.; Li X. Porous membranes in secondary battery technologies. *Chem. Soc. Rev.* **2017**, 46, 2199-2236.
7. Chu F.; Kimura Y. Structure and gas permeability of microporous films prepared by biaxial drawing of β-form polypropylene. *Polymer* **1996**, 37, 573-579.
8. Luo B.; Li Z.; Zhang J.; Wang X. Formation of anisotropic microporous isotactic polypropylene (iPP) membrane via thermally induced phase separation. *Desalination* **2008**, 233, 19-31.
9. Zeng F.; Xu R.; Ye L.; Xiong B.; Kang J.; Xiang M.; Li L.; Sheng X.; Hao Z. Effects of Heat Setting on the Morphology and Performance of Polypropylene Separator for Lithium Ion Batteries. *Industrial & Engineering Chemistry Research* **2019**, 58, 2217-2224.
10. Ruijie X.; Jiayi X.; Ziqin T.; Henghui H.; Xiande C.; Caihong L.; Xingqi Z. Pore

growth and stabilization in uniaxial stretching polypropylene microporous membrane processed by heat-setting. *J. Polym. Sci., Part B: Polym. Phys.* **2018**, 56, 1604-1614.

11. Wu T.; Xiang M.; Cao Y.; Kang J.; Yang F. Pore formation mechanism of β nucleated polypropylene stretched membranes. *RSC Adv.* **2014**, 4, 36689-36701.
12. Wu G.-G.; Chen W.-B.; Ding C.; Xu L.-Y.; Liu Z.-Y.; Yang W.; Yang M.-B. Pore formation mechanism of oriented β polypropylene cast films during stretching and optimization of stretching methods: In-situ SAXS and WAXD studies. *Polymer* **2019**, 163, 86-95.
13. Li J. X.; Cheung W. L.; Chan C. M. On deformation mechanisms of β-polypropylene 2. Changes of lamellar structure caused by tensile load. *Polymer* **1999**, 40, 2089-2102.
14. Lee H.; Yanilmaz M.; Toprakci O.; Fu K.; Zhang X. A review of recent developments in membrane separators for rechargeable lithium-ion batteries. *Energy Environ. Sci.* **2014**, 7, 3857-3886.
15. Wu G.-G.; Ding C.; Chen W.-B.; Zhang Y.; Yang W.; Yang M.-B. Effect of the content of β form crystals on biaxially stretched polypropylene microporous membranes and the tuning of pore structures. *Polymer* **2019**, 175, 177-185.
16. Zhang D.; Ding L.; Yang F.; Lan F.; Cao Y.; Xiang M. Effect of annealing on the microvoid formation and evolution during biaxial stretching of β nucleated isotactic polypropylene. *Polymer-Plastics Technology and Materials* **2020**, 59, 1595-1607.
17. Zhang C.; Liu G.; Song Y.; Zhao Y.; Wang D. Structural evolution of β – iPP during uniaxial stretching studied by in–situ WAXS and SAXS. *Polymer* **2014**, 55, 6915-6923.
18. Xiande C.; Ruijie X.; Jiayi X.; Yuanfei L.; Caihong L.; Liangbin L. The study of room-temperature stretching of annealed polypropylene cast film with row-nucleated crystalline structure. *Polymer* **2016**, 94, 31-42.
19. Wu G.-G.; Xu L.-Y.; Chen W.-B.; Ding C.; Liu Z.-Y.; Yang W.; Yang M.-B. Oriented polypropylene cast films consisted of β-transcrystals induced by the

nucleating agent self-assembly and its homogeneous membranes with high porosity. *Polymer* **2018**, 151, 136-144.

20. Sadeghi F.; Ajji A.; Carreau P. Analysis of microporous membranes obtained from polypropylene films by stretching. *J. Membr. Sci.* **2007**, 292, 62-71.
21. Lyu D.; Chen R.; Lu Y.; Men Y. Subsequent but Independent Cavitation Processes in Isotactic Polypropylene during Stretching at Small- and Large-Strain Regimes. *Industrial & Engineering Chemistry Research* **2018**, 57, 8927-8937.
22. Lin Y.; Chen W.; Meng L.; Wang D.; Li L. Recent advances in post-stretching processing of polymer films with in situ synchrotron radiation X-ray scattering. *Soft Matter* **2020**, 16, 3599-3612.
23. Li S.; Zheng G.; Jia Z.; Zhang Z.; Liu C.; Chen J.; Li Q.; Shen C.; Peng X. Effect of Stretching on β-Phase Content of Isotactic Polypropylene Melt Containing β-Nucleating Agent. *Journal of Macromolecular Science, Part B* **2011**, 51, 828-838.
24. Offord G. T.; Armstrong S. R.; Freeman B. D.; Baer E.; Hiltner A.; Swinnea J. S.; Paul D. R. Porosity enhancement in β nucleated isotactic polypropylene stretched films by thermal annealing. *Polymer* **2013**, 54, 2577-2589.
25. Wu T.; Xiang M.; Cao Y.; Yang F. Influence of annealing on stress–strain behaviors and performances of β nucleated polypropylene stretched membranes. *Journal of Polymer Research* **2014**, 21.
26. Yang S.; Gu J.; Yin Y. A biaxial stretched β-isotactic polypropylene microporous membrane for lithium-ion batteries. *J. Appl. Polym. Sci.* **2018**, 135.
27. Yang F.; Wu T.; Xiang M.; Cao Y. Deformation and pore formation mechanism of β nucleated polypropylene with different supermolecular structures. *Eur. Polym. J.* **2017**, 91, 134-148.
28. Ding L.; Ge Q.; Xu G.; Wu T.; Yang F.; Xiang M. Influence of oriented β-lamellae on deformation and pore formation in β-nucleated polypropylene. *J. Polym. Sci., Part B: Polym. Phys.* **2017**, 55, 1745-1759.
29. Zhu Y.; Zhao Y.; Fu Q. Toward uniform pore-size distribution and high porosity

 doi:10.20944/preprints202010.0359.v1

of isotactic polypropylene microporous membrane by adding a small amount of ultrafine full-vulcanized powder rubber. *Polymer* **2016**, 103, 405-414.

30. Bao R.; Ding Z.; Zhong G.; Yang W.; Xie B.; Yang M. Deformation-induced morphology evolution during uniaxial stretching of isotactic polypropylene: effect of temperature. *Colloid. Polym. Sci.* **2011**, 290, 261-274.
31. Bao R.-Y.; Ding Z.-T.; Liu Z.-Y.; Yang W.; Xie B.-H.; Yang M.-B. Deformation-induced structure evolution of oriented β-polypropylene during uniaxial stretching. *Polymer* **2013**, 54, 1259-1268.
32. Kurihara H.; Kitade S.; Ichino K.; Akiba I.; Sakurai K. Elongation induced β- to α-crystalline transformation and microvoid formation in isotactic polypropylene as revealed by time-resolved WAXS/SAXS. *Polym. J.* **2018**, 51, 199-209.
33. Chen Q.; Wang Z.; Zhang S.; Cao Y.; Chen J. Structure Evolution and Deformation Behavior of Polyethylene Film during Biaxial Stretching. *ACS Omega* **2020**, 5, 655-666.
34. Jariyasakoolroj P.; Tashiro K.; Wang H.; Yamamoto H.; Chinsirikul W.; Kerddonfag N.; Chirachanchai S. Isotropically small crystalline lamellae induced by high biaxial-stretching rate as a key microstructure for super-tough polylactide film. *Polymer* **2015**, 68, 234-245.
35. Chen Z.; Kang W.; Kang J.; Chen J.; Yang F.; Cao Y.; Xiang M. Non-isothermal crystallization behavior and melting behavior of Ziegler–Natta isotactic polypropylene with different stereo-defect distribution nucleated with bi-component β-nucleation agent. *Polym. Bull.* **2015**, 72, 3283-3303.
36. Chen X.; Lv F.; Su F.; Ji Y.; Meng L.; Wan C.; Lin Y.; Li X.; Li L. Deformation mechanism of iPP under uniaxial stretching over a wide temperature range: An in-situ synchrotron radiation SAXS/WAXS study. *Polymer* **2017**, 118, 12-21.
37. Bai H.; Wang Y.; Zhang Z.; Han L.; Li Y.; Liu L.; Zhou Z.; Men Y. Influence of Annealing on Microstructure and Mechanical Properties of Isotactic Polypropylene with β-Phase Nucleating Agent. *Macromolecules* **2009**, 42, 6647-6655.

 doi:10.20944/preprints202010.0359.v1

38. Xiong B.; Kang J.; Chen R.; Men Y. Initiation of cavitation upon drawing of pre-oriented polypropylene film: In situ SAXS and WAXD studies. *Polymer* **2017**, 128, 57-64.

39. Jones A. T.; Aizlewood J. M.; Beckett D. R. Crystalline Forms of Isotactic Polypropylene. *Makromolekul Chem* **1964**, 75, 134-158.

40. Hermans P. H.; Platzek P. Beitrge zur Kenntnis des Deformationsmechanismus und der Feinstruktur der Hydratzellulose. *Kolloid-Zeitschrift* **1939**, 88, 68-72.

41. Lu X.; Li X. Preparation of polyvinylidene fluoride membrane via a thermally induced phase separation using a mixed diluent. *J. Appl. Polym. Sci.* **2009**, 114, 1213-1219.

42. Fischer S.; Diesner T.; Rieger B.; Marti O. Simulating and evaluating small-angle X-ray scattering of micro-voids in polypropylene during mechanical deformation. *J. Appl. Crystallogr.* **2010**, 43, 603-610.

43. Sun W.; Chen T.; Chen C.; Li J. A study on membrane morphology by digital image processing. *J. Membr. Sci.* **2007**, 305, 93-102.